Research Square

Preprints are preliminary reports that have not undergone peer review.
They should not be considered conclusive, used to inform clinical practice,
or referenced by the media as validated information.

Mechanical Frequency Combs via Three-Wave-Mixing Parametric Excitation: A Scalable Inertial-Sensing Modality

Zihuan Liu

zihuanliu@utexas.edu

The University of Texas at Austin

Xingwei Gao

The University of Texas at Austin

Yen-Chen Wang

The University of Texas at Austin

Xiaoyu Niu

The University of Texas at Austin

Ehsan Vatankhah

The University of Texas at Austin

Meng Kang

City University of New York

Shivansh Madan

The University of Texas at Austin

Yuqi Meng

The University of Texas at Austin

Ruochen Lu

The University of Texas at Austin

Andrea Alù

City University of New York

David Burghoff

The University of Texas at Austin

Neal Hall

The University of Texas at Austin

Article

Keywords: MEMS, frequency comb, three-wave mixing, parametric excitation, inertial sensing, coupled-mode theory, PZT

Posted Date: September 15th, 2026

DOI: https://doi.org/10.21203/rs.3.rs-10820398/v1

License: This work is licensed under a Creative Commons Attribution 4.0 International License.
Read Full License

Additional Declarations: No competing interests reported.

Mechanical Frequency Combs via Three-Wave-Mixing Parametric Excitation: A Scalable Inertial-Sensing Modality

Zihuan Liu[1*†], Xingwei Gao[1†], Yen-Chen Wang[1], Xiaoyu Niu[1], Ehsan Vatankhah[1], Meng Kang[2], Shivansh Madan[1], Yuqi Meng[1], Ruochen Lu[1], Andrea Alù[2], David Burghoff[1], Neal A. Hall[1*]

[1*]Chandra Family Department of Electrical and Computer Engineering, The University of Texas at Austin, Austin, TX, USA.
[2]Photonics Initiative, Advanced Science Research Center, The City University of New York, New York, NY, USA.

*Corresponding author(s). E-mail(s): zihuanliu@utexas.edu; nahall@utexas.edu;
†These authors contributed equally to this work.

Abstract

Resonant microelectromechanical-system (MEMS) accelerometers built on a single vibrational mode face a $\boldsymbol{Q}$–bandwidth trade-off: frequency stability and measurement bandwidth cannot be improved together. Here we report that a clamped–clamped lead-zirconate-titanate (PZT)-on-silicon bridge self-sustains a mechanical frequency comb through three-wave-mixing parametric excitation, with no oscillator or feedback electronics, and we use the comb itself to sense acceleration. We measure the comb experimentally and map its parametric-instability (Arnold-tongue) threshold. External acceleration axially loads the bridge through mid-plane stretching and frequency-modulates the comb while the fixed pump stays unmodulated; per-comb-line frequency-modulation (FM) demodulation resolves the applied acceleration tone on all seven mechanical comb lines simultaneously—each an independent channel—with frequency deviation growing with overtone order. A two-stage coupled-mode-theory framework reproduces the comb spectrum, instability threshold, and FM response end-to-end. Because the comb is sustained by a nonlinear attractor rather than the $\boldsymbol{Q}$ of one resonance, it offers a route to inertial sensing beyond the single-mode trade-off.

Keywords: MEMS, frequency comb, three-wave mixing, parametric excitation, inertial sensing, coupled-mode theory, PZT

1 Introduction

High-precision inertial applications—autonomous navigation, geodesy, and seismic monitoring—demand simultaneously low noise, wide bandwidth, and large dynamic range from a single accelerometer [1–4]. A single-mode resonator forces a Q–bandwidth trade-off: improving frequency stability requires high Q, while wide bandwidth requires low Q. The two requirements cannot be reconciled within the single-harmonic-oscillator (SHO) framework [5, 6]. Three-wave-mixing parametric excitation (3WM-PE) provides an alternative readout architecture that relaxes this single-mode Q–bandwidth compromise. Phase-sensitive parametric gain reduces effective damping and redistributes noise between quadratures [7, 8], and three-wave coupling enforces phase coherence across all comb lines, so the resulting oscillation is sustained by a nonlinear attractor rather than by the Q of a single resonance. Robust operation of piezoelectric microelectromechanical-system (MEMS) resonators deep in nonlinear regimes has recently been demonstrated experimentally [9].

Optical frequency combs transformed spectroscopy by delivering many phase-coherent tones from a single oscillator [10, 11]. Transplanted into the mechanical domain, this turns each comb line into an independent inertial-sensing channel [12–15]. Mechanical combs are most naturally produced by 3WM-PE: a single fixed-frequency pump couples two eigenmodes parametrically, and the resulting Arnold-tongue instability produces a self-sustained carrier with symmetric sidebands spaced by the modal difference frequency, with no external oscillator or feedback loop

required [16, 17]. Frequency-comb generation via this mechanism has now been demonstrated across a range of MEMS, nanoelectromechanical-system (NEMS), and acoustic platforms [18–22].

Here we report three results on a single lead-zirconate-titanate (PZT)-on-silicon bridge platform: controlled generation of a self-sustained phononic comb via 3WM-PE; a two-stage coupled-mode-theory framework that quantitatively reproduces the comb spectrum, the Arnold-tongue instability threshold, and the frequency-modulation (FM) response; and an end-to-end accelerometer demonstration in which per-comb-line FM demodulation of the laser-Doppler-vibrometer (LDV) signal resolves the applied acceleration tone on all seven mechanical comb lines simultaneously. We present this as a demonstration that the 3WM comb transduces acceleration, not as a competitive figure of merit: the prototype is sensitivity-limited by the 14 µm bridge thickness (flexural-stiffness-dominated regime) and by off-chip instrumentation noise, both addressable in subsequent device generations.

Figure 1 outlines this sensing modality end to end. A single fixed-frequency pump applied to the PZT layer parametrically couples two eigenmodes of the clamped–clamped bridge through the energy-conserving three-wave-mixing condition $\omega_p \approx \omega_1 + \omega_2$ (Fig. 1a). Above the parametric-instability threshold, the coupled pair settles onto a stable limit cycle and the bridge self-sustains a phase-coherent mechanical frequency comb—harmonics of Mode 1, the Mode-2 carrier, and its sideband family—with no external oscillator, phase-locked loop, or feedback electronics (Fig. 1b). External acceleration axially loads the bridge through mid-plane stretching and frequency-modulates every mechanical comb line simultaneously, while the fixed pump stays unmodulated; per-comb-line FM demodulation of the LDV velocity record therefore recovers the input acceleration on each line as an independent channel, with FM deviation growing with overtone order n (Fig. 1c). The following sections establish each stage of this chain experimentally and theoretically.

2 Results

Device platform and modal landscape

The device is a clamped–clamped MEMS bridge with a PZT-on-silicon-on-insulator (SOI) layer stack and a central proof mass; the bridge footprint is 6.70 mm, and the 2 µm PZT layer is used purely for electromechanical actuation, with the mechanical response read out optically via LDV. Three nominally identical dies from the same platform are measured: Device A (linear characterization and threshold mapping, Figs. 2 and 4) with $f_1 \approx 3.21$ kHz, $f_2 \approx 94.91$ kHz, and a parametric pump at $\omega_p/2\pi \approx 98.30$ kHz; Device B (accelerometer demonstration, Figs. 5 and 6) with $f_1 \approx 3.49$ kHz, $f_2 \approx 102.70$ kHz, and a parametric pump at $\omega_p/2\pi \approx 106.19$ kHz; and Device C (comb-spectrum measurement, Fig. 3) with $f_1 \approx 3.61$ kHz and $f_2 \approx 130.11$ kHz. In each device the pump frequency is set by that device's own modal sum through the three-wave-mixing condition $\omega_p \approx \omega_1 + \omega_2$; the pump frequencies therefore differ from die to die, reflecting unit-to-unit variation and the mode pair engaged for comb generation in each die.

The small-signal LDV velocity spectrum on Device A (Fig. 2c, grey) is overlaid with an 18-mode linear temporal coupled-mode theory (TCMT) fit (red) across 0–400 kHz; the fit reproduces every observable peak in the spectrum and yields the linear angular frequencies ω_n and damping rates r_n that are subsequently consumed by the nonlinear two-mode coupled-mode theory (CMT) (details in Materials and methods). The same fitting procedure, applied to the small-signal spectrum of each die, supplies the linear modal parameters of Devices B and C. Full-field LDV mode shapes (Fig. 2d) identify the 3WM pair: a low-frequency proof-mass / bridge mode at 3.21 kHz ($\omega_1/2\pi$) and a higher-order bending mode at 94.91 kHz ($\omega_2/2\pi$) that together satisfy the three-wave-mixing condition $\omega_p \approx \omega_1 + \omega_2$ for pumping near 98.30 kHz. The Device-B small-signal LDV measurement used to set the FM-transduction operating point—including the voltage-scaled peak velocities of the Device-B Mode 1 and pump lines—is given in Supplementary Note S1 (Fig. S1).

Self-sustained frequency-comb generation

Above the parametric instability threshold, the LDV velocity spectrum of Device C exhibits the comb fingerprint: three line families, comprising harmonics of ω_1 at low frequency, a carrier-plus-sideband cluster at $\omega_2 \pm n\,\omega_1$, and a second-harmonic cluster at $2\omega_2 \pm n\,\omega_1$ (Fig. 3c). The comb-line set used for the accelerometer demodulation chain below — Mode 1, 2·Mode 1, 3·Mode 1, 4·Mode 1, Mode 2 − Mode 1, Mode 2, Pump + Mode 1, and the pump — is independently resolved here. The two-mode nonlinear CMT (Materials and methods) reproduces the measured spectrum line-for-line: numerical integration of Eqs. (1)–(2) yields per-mode steady-state spectra for v_1 and v_2 (Fig. 3a, red and green respectively) whose coherent sum (Fig. 3b) reconstructs the measured carrier and sideband families (Fig. 3c) over the full 0–300 kHz band. The agreement — including the second-harmonic family at $2\omega_2$, a direct signature of the quadratic self-coupling $\alpha_{22}x_2^2$ — confirms that quadratic ($\chi^{(2)}$-type) nonlinearity alone accounts for comb generation in the experimental regime accessed here; no cubic terms are required to reproduce the measured line set. Close inspection of Fig. 3b,c also reveals weak spectral features around $\omega_2 \pm n\,\omega_1$ and $2\omega_2 \pm n\,\omega_1$ that appear in only one of the two panels. The two-mode model retains only the two modes responsible for comb formation, so weak features in the measured spectrum that arise from residual excitation of other linear modes of the bridge (cf. Fig. 2c), from higher-order mixing

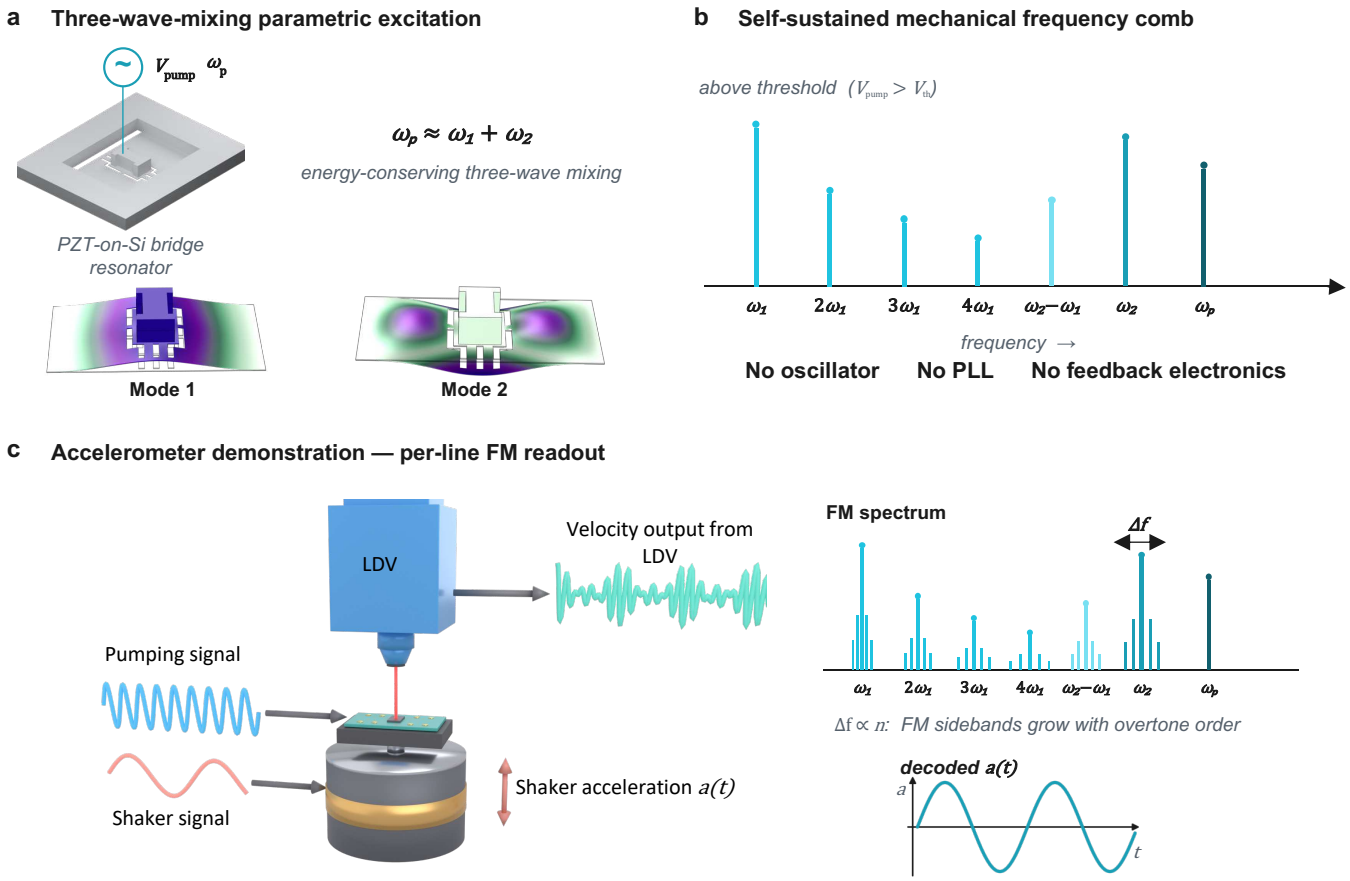


Fig. 1 Three-wave-mixing frequency-comb accelerometer: concept and end-to-end readout chain. (**a**) Three-wave-mixing parametric excitation (3WM-PE). A single pump tone at ω_p (amplitude V_{pump}), applied to the PZT layer of a clamped–clamped PZT-on-silicon bridge resonator, parametrically couples two eigenmodes of the bridge—a low-frequency proof-mass / bridge mode (Mode 1, at ω_1) and a higher-order bending mode (Mode 2, at ω_2)—through the energy-conserving three-wave-mixing condition $\omega_p \approx \omega_1 + \omega_2$. Simulated mode shapes of the two coupled modes are shown below the device rendering. (**b**) Above the parametric-instability threshold ($V_{\mathrm{pump}} > V_{\mathrm{th}}$) the coupled pair settles onto a stable limit cycle and the bridge self-sustains a phase-coherent mechanical frequency comb (schematic): harmonics of Mode 1 at $n\omega_1$, the difference line at $\omega_2 - \omega_1$, the Mode-2 carrier at ω_2, and residual feedthrough at the pump ω_p. No external oscillator, phase-locked loop, or feedback electronics is required. (**c**) Accelerometer demonstration by per-comb-line FM readout. The device is mounted on a shaker and driven only by the fixed pump; a laser Doppler vibrometer (LDV) records the velocity output. Shaker acceleration $a(t)$ axially loads the bridge through mid-plane stretching and frequency-modulates every mechanical comb line simultaneously (sidebands $\pm\Delta f$), with peak FM deviation growing with overtone order n ($\Delta f \propto n$), while the pump line stays unmodulated. Per-line FM demodulation of any comb line recovers $a(t)$, making each comb line an independent inertial channel.

among comb lines, and from instrumentation feedthrough have no counterpart in the simulation; conversely, the noiseless simulation resolves high-order sidebands whose measured counterparts fall below the experimental noise floor. These unmatched features carry negligible power relative to the eight resolved comb lines and do not affect the line-for-line agreement reported above.

Parametric threshold and Arnold tongue

The numerical phase diagram in (Γ, ω_p) from integration of the two-mode CMT (Fig. 4a) reproduces the analytical Arnold-tongue boundary derived in Materials and methods by truncating the Floquet expansion to the dominant Fourier components $m = -1, 0, 1$ (Eq. (20)). The experimental velocity power-spectral-density (PSD) heatmap (Fig. 4b) exhibits a threshold boundary with the same characteristic tongue shape in the (V_p, ω_p) plane; the two boundaries are not expected to coincide when plotted against raw pump voltage, because the conversion from applied voltage to effective parametric coupling is itself frequency dependent. The $(V_p, \omega_p) \to \Gamma$ mapping calibrated in Fig. 4c quantifies this conversion and carries Eq. (20) directly into the experimental control parameters (voltages are reported at the piezo-amplifier output). Two orthogonal cuts through the tongue confirm the picture. Fixing the pump frequency at $\omega_p/2\pi = 98.30\,\mathrm{kHz}$ and sweeping the pump voltage from 0 to 10 V resolves a clean-to-comb bifurcation at $V_p \approx 4.5\,\mathrm{V}$ (Fig. 4d): below threshold the spectrum is featureless, while above threshold the full comb appears abruptly across the band. Fixing the pump

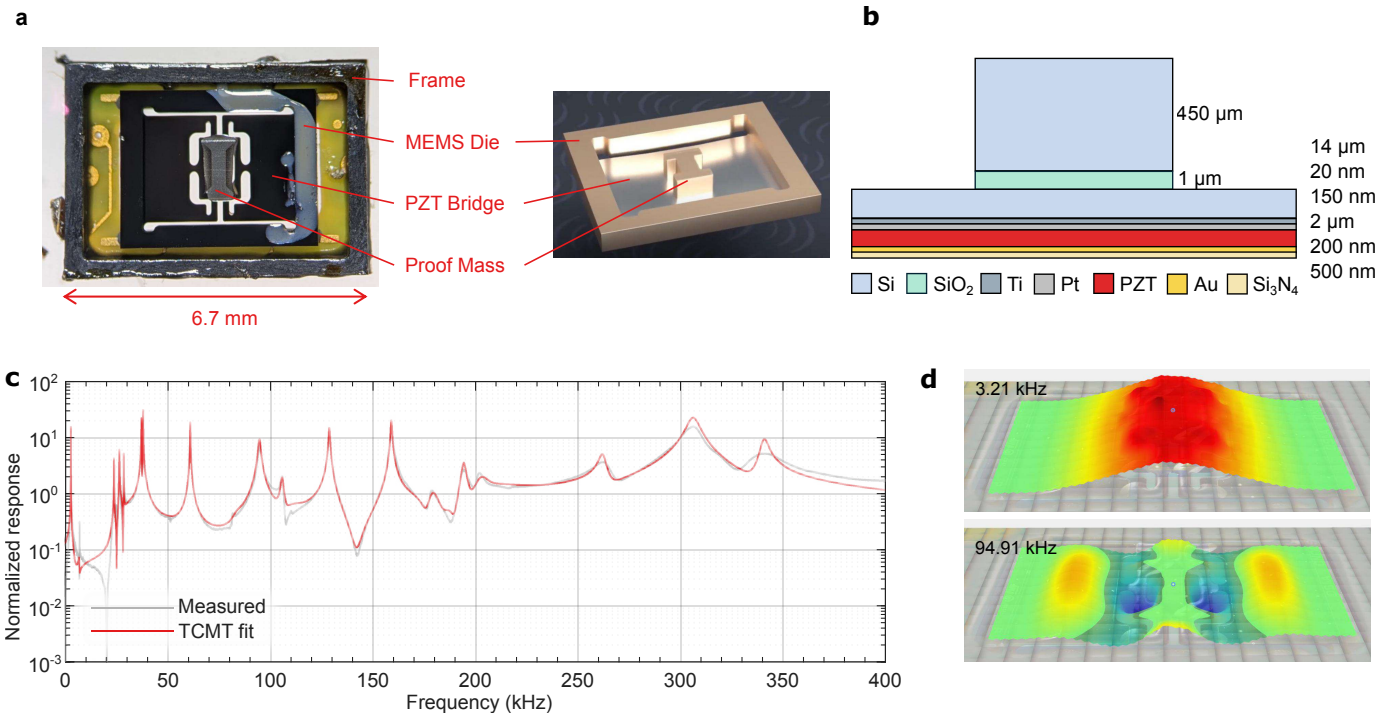


Fig. 2 Device overview. (**a**) Photograph of the packaged MEMS die and CAD rendering of the PZT-on-silicon clamped–clamped bridge with central proof mass; bridge footprint 6.70 mm. (**b**) Cross-sectional schematic of the device stack, bottom-to-top: Si handle (450 µm) / SiO_2 buried oxide (BOX, 1 µm) / device Si (14 µm) / Ti adhesion (20 nm) / Pt bottom electrode (150 nm) / PZT active layer (2 µm) / Au top electrode (200 nm) / Si_3N_4 passivation (500 nm). (**c**) Measured small-signal LDV velocity response (grey), normalized to its broadband mean, overlaid with the 18-mode linear temporal coupled-mode theory (TCMT) fit (red) across 0–400 kHz on Device A; the normalized response is plotted on a log scale, 10^{-3}–10^{2}. The fit reproduces every observable peak in the spectrum and supplies the linear angular frequencies ω_n and damping rates r_n used as inputs to the nonlinear two-mode CMT; the same fitting procedure, applied to each device's small-signal spectrum, supplies the linear parameters of Devices B and C. (**d**) Experimentally mapped (full-field scanning LDV) mode shapes of Device A at 3.21 kHz (fundamental proof-mass / bridge mode) and 94.91 kHz (higher-order bending mode used as the parametric idler).

voltage at 6.00 V and sweeping the pump frequency across 96.5–100.0 kHz (Fig. 4e) confines the comb-active band to a narrow window around $\omega_p/2\pi \approx 98.30$ kHz, i.e. the V-shaped Arnold tongue narrowing back to threshold on either side.

Per-comb-line FM transduction of acceleration

The fixed-frequency pump itself is never modulated by acceleration; only the mechanical eigenfrequencies are. Inertial loading axially shifts ω_1 and ω_2 through mid-plane stretching, and these shifts are imprinted on every comb line $\omega_p \pm n\,\omega_1$ simultaneously. Because the pump is constant and the comb structure is set by ω_1, ω_2, the transduction is intrinsically FM: time-domain envelopes are almost flat under varying acceleration, so acceleration couples cleanly into instantaneous frequency with little amplitude dynamics corrupting the readout [14, 23].

We validate the transduction on Device B with a calibrated electromagnetic shaker (setup photograph in Supplementary Note S2, Fig. S2). The above-threshold Device-B comb spectrum under these pump conditions, which sets the carrier and sideband family that the FM-demodulation pipeline operates on, is reported in Supplementary Note S1, Fig. S1(b). LDV velocity records are processed offline: each of the eight resolved comb lines is isolated by a matched-filter finite-impulse-response (FIR) bandpass before instantaneous-frequency extraction (full pipeline in Materials and methods). The bandpass step is illustrated in Fig. 5: panel (a) overlays the raw measured spectrum (grey), the band-passed spectrum that feeds the FM demodulator (blue), and the FIR filter shape (red dashed) for each of the eight sub-bands; panel (b) applies the same filter bank to the simulated FM velocity spectra from the two-mode nonlinear CMT, demonstrating that the pipeline acts on the simulated and measured records identically.

Under a 50 Hz sinusoid producing peak acceleration $\approx \pm 100\,\mathrm{m\,s^{-2}}$ ($\approx \pm 10\,g$) at the device, the demodulated frequency-deviation traces (Fig. 6a) reproduce the applied-acceleration trace (red, rightmost sub-panel of Fig. 6a) on every mechanical comb line, and the corresponding demodulated frequency-domain spectra (Fig. 6c) show a clean 50 Hz peak on every mechanical line. The "Pump" sub-panel of Fig. 6(a,c) is flat at the noise floor: the pump itself is unmodulated by acceleration, and only the mechanical eigenfrequencies respond. This is direct evidence of FM-only encoding. Simulated demodulated time-domain traces (Fig. 6b) and frequency-domain spectra (Fig. 6d) reproduce, comb-line by comb-line, the measured chain—validating the acceleration-encoding mechanism end-to-end across all eight comb lines simultaneously. The mechanical scale factor on the Mode-1 carrier is 1 Hz/g. Because the pump frequency is

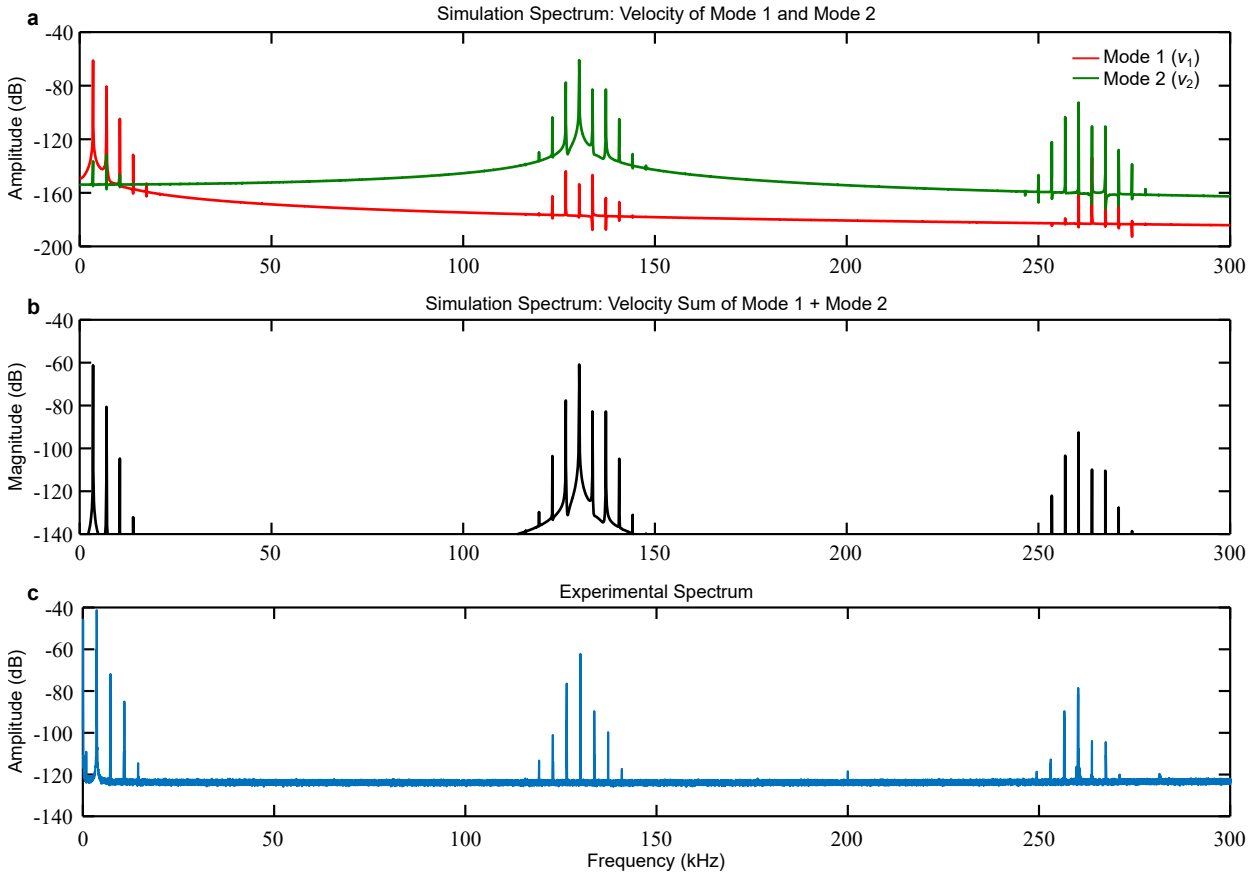


Fig. 3 Two-mode nonlinear CMT reproduces the measured frequency-comb spectrum on Device C. (**a**) Simulated steady-state velocity spectra from numerical integration of Eqs. (1)–(2), plotted separately for Mode 1 (v_1, red, $\omega_1/2\pi \approx 3.61\,\mathrm{kHz}$) and Mode 2 ($v_2$, green, $\omega_2/2\pi \approx 130.11\,\mathrm{kHz}$) under pumping at $\omega_p \approx \omega_1 + \omega_2$ above threshold. (**b**) Steady-state Fourier spectrum of the coherent sum $v_1 + v_2$ from (**a**), reproducing the carrier-plus-sideband comb structure $\omega_2 \pm n\,\omega_1$ that is directly observed in measurement. (**c**) Measured LDV velocity spectrum on Device C (a separate die from the Device-A threshold mapping of Fig. 4) under matched pumping conditions, plotted on identical axes for one-to-one overlay against (**b**). The Mode-2 carrier, the equispaced sideband family at $\omega_2 \pm n\,\omega_1$, and the residual feedthrough at the pump are all reproduced by the simulation without per-line tuning.

externally fixed and the three-wave-mixing condition $\omega_p \approx \omega_1 + \omega_2$ is maintained by the self-sustained comb dynamics, $\delta\omega_p = 0$ forces $\delta\omega_2 = -\delta\omega_1$: the Mode-2 carrier shifts with the same magnitude as Mode 1 but 180° out of phase. The overtone lines at $n\omega_1$ accumulate n copies of the Mode-1 shift, so the deviation amplitude grows as $n \cdot (1\,\mathrm{Hz/g})$, reaching apparent slopes of 2 Hz/g, 3 Hz/g, and 4 Hz/g at $n = 2, 3, 4$ respectively (Fig. 6b; the measured trace at $n = 4$ is examined under *Overtone-comb scaling* below). These overtone slopes are kinematic amplifications of the same Mode-1 frequency shift rather than independent sensor channels; the multi-comb SNR gain available from coherently combining them is treated separately below.

Overtone-comb scaling and multi-comb readout

The n-th-order comb line at $\omega_2 + n\,\omega_1$ shifts by $\delta\omega_2(a) + n\,\delta\omega_1(a)$ under axial load, so the FM deviation of overtone lines should grow approximately linearly with n [15]. The simulated FM deviation (Fig. 6b) follows this prediction cleanly, growing from $\approx \pm 10\,\mathrm{Hz}$ at $n = 1$ (Mode 1) to $\approx \pm 40\,\mathrm{Hz}$ at $n = 4$ (4·Mode 1) in agreement with the kinematic $n \cdot k_{\mathrm{sf},1}$ scaling. The measured deviations (Fig. 6a) track the simulation through $n \leq 3$, but the 4·Mode 1 trace exhibits excess noise because the smaller amplitude of the 4·Mode 1 line in the LDV spectrum (Fig. 5a) degrades the signal-to-noise ratio (SNR) of its demodulated time series. The Mode-2 − Mode-1 line does not cleanly track the applied acceleration for the same reason: the Mode-2 demodulated trace is itself noisy, and that noise carries into the difference line. The Pump + Mode 1 line shows a similar excess in its measured peak deviation (34.9 Hz in Fig. 6a versus the simulated 11.2 Hz in Fig. 6b), again traceable to the lower above-threshold amplitude of that line in the LDV spectrum (Fig. 5a); its acceleration-coherent component is quantified by the 50 Hz peak in Fig. 6c. With N simultaneously measured comb lines, coherent combining offers an SNR gain up to $\sqrt{N}$ for uncorrelated noise and up to N for correlated (common-mode, pump-phase) noise that can be differentially canceled. Because per-line FM deviation grows with n, higher-order comb lines reach the edge of the demodulation window at lower input acceleration than the carrier; selecting lower-order lines therefore extends the usable input range. These two readout levers—overtone scaling and multi-comb combining—are

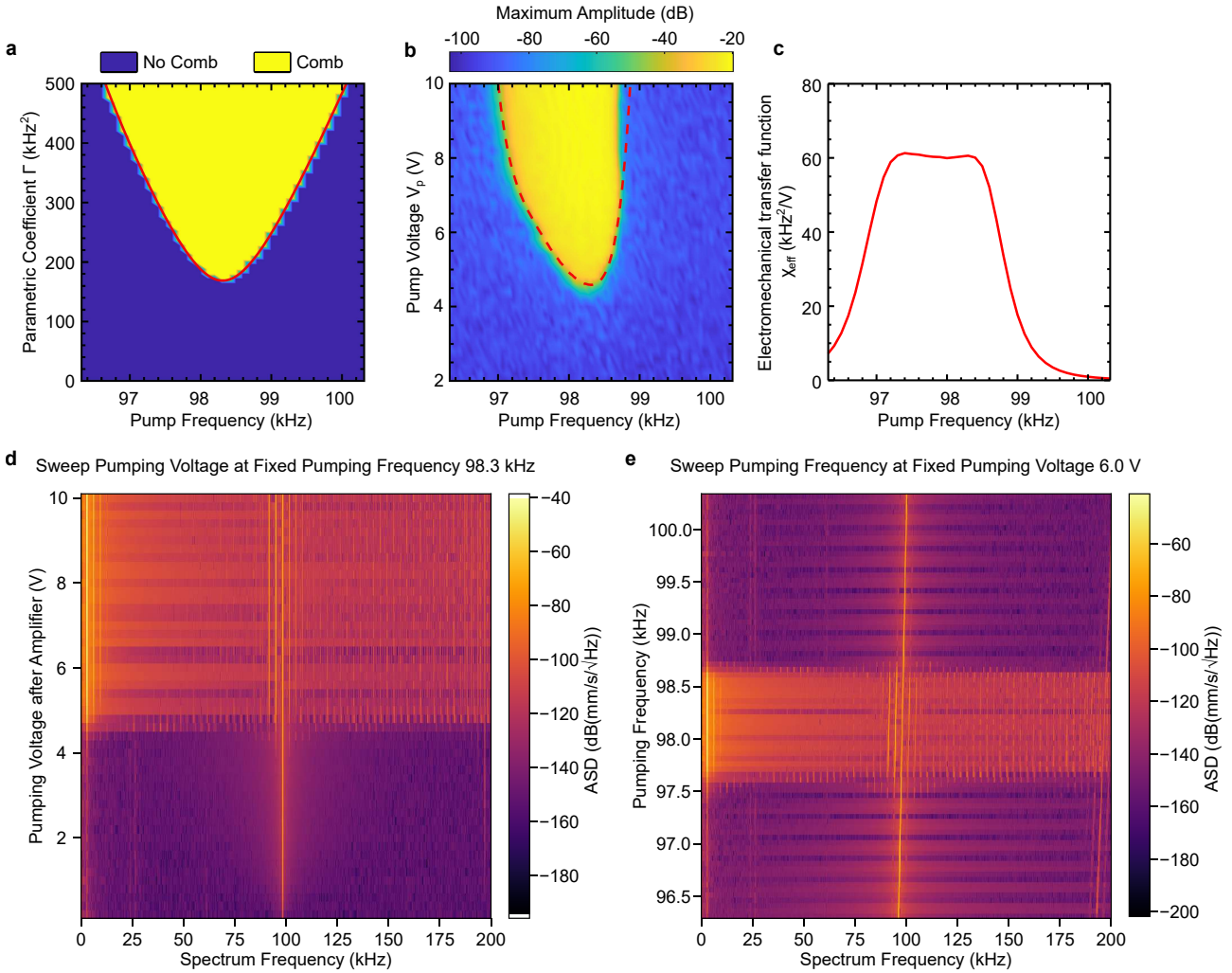


Fig. 4 Parametric instability threshold and Arnold tongue (Device A). (**a**) Steady-state phase diagram in the (Γ, ω_p) parameter space, obtained from numerical integration of the two-mode nonlinear CMT [Eqs. (1)–(2)]. The red curve overlays the analytical Arnold-tongue boundary obtained from the truncated-Floquet threshold condition (Eq. (20)). (**b**) Experimental velocity-PSD heatmap as a function of pump frequency ω_p and pump voltage V_p (after the piezo amplifier). The dashed red curve traces the experimentally measured threshold separating the no-comb and comb regions. (**c**) Frequency-dependent electromechanical transfer function $\chi_{\mathrm{eff}}(\omega_p)$ extracted from the analytical threshold $\Gamma_{\mathrm{th}}(\omega_p)$ in panel (**a**) and the experimentally measured threshold voltage $V_{\mathrm{th}}(\omega_p)$ in panel (**b**) through Eq. (21). The non-flat response demonstrates that the effective parametric coupling depends on the pump frequency. (**d**) Velocity-spectrum heatmap versus pump voltage at fixed pump frequency $\omega_p/2\pi = 98.30\,\mathrm{kHz}$. The y-axis is the pump voltage at the amplifier output (0–10 V); a sharp clean-to-comb bifurcation at $V_p \approx 4.5\,\mathrm{V}$ is directly visible as the abrupt appearance of the comb across the horizontal band. (**e**) Velocity-spectrum heatmap versus pump frequency at fixed pump voltage $V_p = 6.00\,\mathrm{V}$ (amplifier output). The comb-active region forms a finite-width window around $\omega_p/2\pi \approx 98.30\,\mathrm{kHz}$, i.e. the projection of the Arnold tongue at the chosen voltage cut.

properties of the comb itself, not of the device-level transducer, and they sit on top of the per-line scale factor reported above.

3 Discussion

The 1 Hz/g carrier scale factor reported above is presented as a proof-of-principle demonstration of the end-to-end transduction chain rather than as a competitive figure of merit. Two limitations explain the modest sensitivity of this prototype. First, the 14 µm bridge is bending-stiffness-dominated rather than tension-dominated: flexural stiffness scales as t^3 while tension stiffness scales as t [24–27], so thinning the beam is the most direct device-level lever to enter the regime where eigenfrequency is sensitive to acceleration-induced axial load. We note that "tension-dominated" here does not imply that the device is operated under a large static tensile preload; rather, it denotes a regime in which small axial-load perturbations produce a larger fractional shift in modal frequency than in the present bending-rigidity-dominated geometry. Finite-element-method (FEM) sensitivity sweeps in Supplementary Note S3 (Fig. S3) trace this $t^3 \to t$ crossover explicitly. Second, the noise floor of the prototype is expected to be limited by pump-source phase noise and offline-demodulation resolution rather than by the mechanical element: the high carrier frequency (≈ 100 kHz Mode 2) and sharp

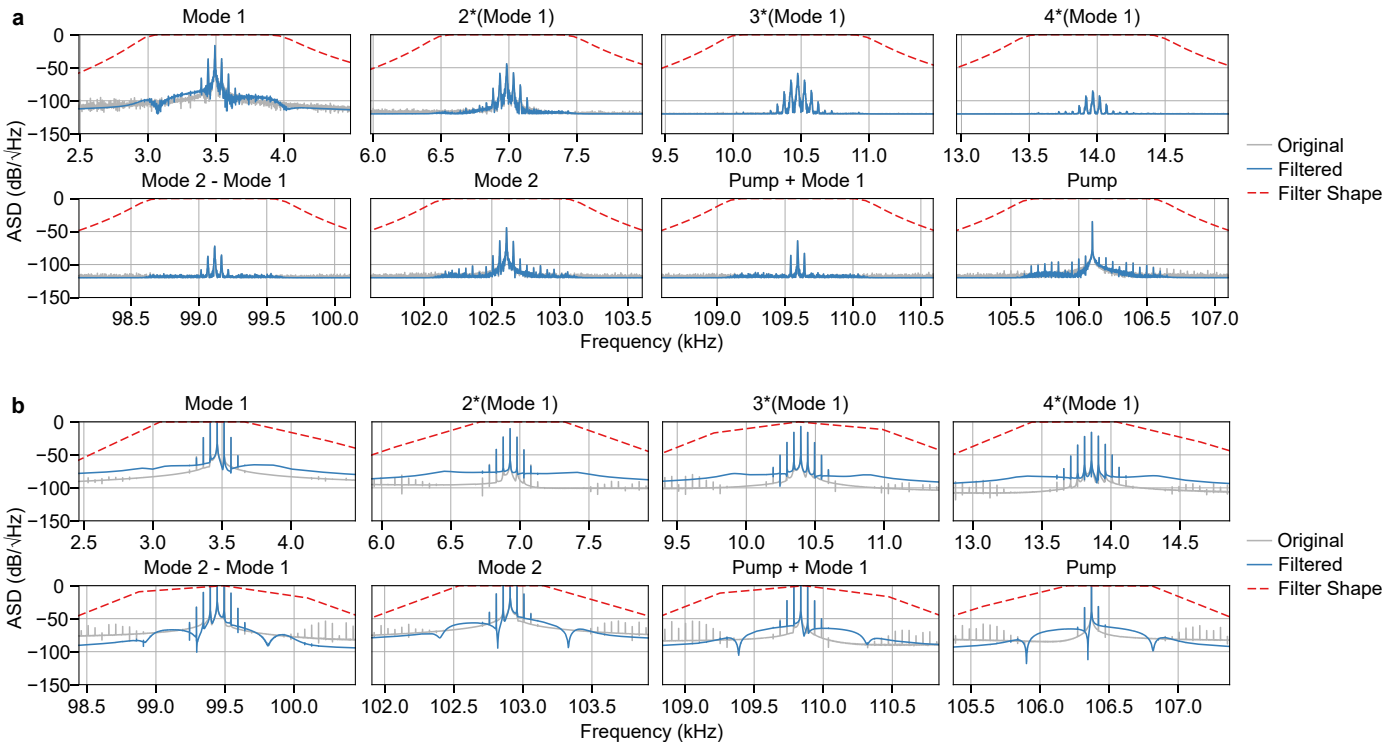


Fig. 5 Per-comb-line postprocessing pipeline: matched-filter isolation of each comb line prior to FM demodulation (Device B). Each of panels (**a**,**b**) is laid out as 8 sub-panels—one per comb line—in the order: Mode 1 ($\omega_1/2\pi \approx 3.49\,\mathrm{kHz}$), 2·Mode 1, 3·Mode 1, 4·Mode 1, Mode 2 − Mode 1, Mode 2 ($\omega_2/2\pi \approx 102.70\,\mathrm{kHz}$), Pump + Mode 1, and Pump ($\omega_p/2\pi \approx 106.19\,\mathrm{kHz}$). The pump satisfies $\omega_p \approx \omega_1 + \omega_2$. In every sub-panel the raw spectrum is shown in grey, the matched-filter-bandpassed spectrum that is fed to the instantaneous-frequency extractor in blue, and the FIR filter shape used to isolate that line in red dashed. (**a**) Measured FM velocity spectra under 50 Hz, $\approx \pm 100\,\mathrm{m\,s^{-2}}$ ($\approx \pm 10\,g$) shaker excitation. (**b**) Simulated FM velocity spectra at the same 8 comb lines from the two-mode nonlinear CMT under matched drive conditions, processed through the same filter bank as (**a**).

parametric threshold produce large above-threshold signal amplitudes, so the dominant noise contribution is external instrumentation rather than the mechanical transducer. A quantitative noise-floor measurement is left for future work. The 3WM paradigm decouples carrier generation (set by nonlinear dynamics, $\omega_p \approx \omega_1 + \omega_2$) from signal encoding (set by axial eigenfrequency sensitivity), so carrier stability and signal dynamic range are not bound by the same Q. Because the comb oscillation settles onto a stable limit cycle, sensor performance is insensitive to loop-filter design and phase-margin constraints—no pump-side feedback electronics are required.

Several scaling levers motivate follow-on work. Reducing the bridge thickness into the tension-dominated regime is the principal device-level lever (Supplementary Note S3). A pump-phase-locked loop is projected to suppress common-mode phase noise by at least an order of magnitude [28] and is a prerequisite for achieving the full multi-comb-N SNR gain. Co-integration of a low-noise transimpedance amplifier and an application-specific integrated circuit (ASIC) FM demodulator would eliminate the dominant instrumentation-noise source and measure the true mechanical noise floor. A differential tuning-fork geometry would offer common-mode rejection [2, 29–31]; proof-mass and bridge-length tuning would amplify the per-g axial-stress response. Multiple resolved bending modes below 400 kHz support several independent 3WM channels, enabling simultaneous multi-axis sensing and cross-comb self-calibration in future device generations. Empirical N-scaling of SNR under multi-comb combining is the natural next experiment.

In summary, on a single PZT-on-Si bridge platform we generate a self-sustained mechanical frequency comb via 3WM-PE; an 18-mode linear TCMT fit feeds a Floquet-treated nonlinear two-mode CMT that quantitatively reproduces the parametric threshold, Arnold-tongue boundary, comb structure, and acceleration-induced FM response; and per-comb-line FM demodulation of the comb readout closes an end-to-end accelerometer chain (1 Hz/g baseline scale factor on the Mode-1 carrier) with the multi-comb modality directly observed. The path to higher sensitivity and lower noise—bridge thinning into the tension-dominated regime, closed-loop pump control, and integrated readout—is identified at the device-physics level rather than at the system-engineering level.

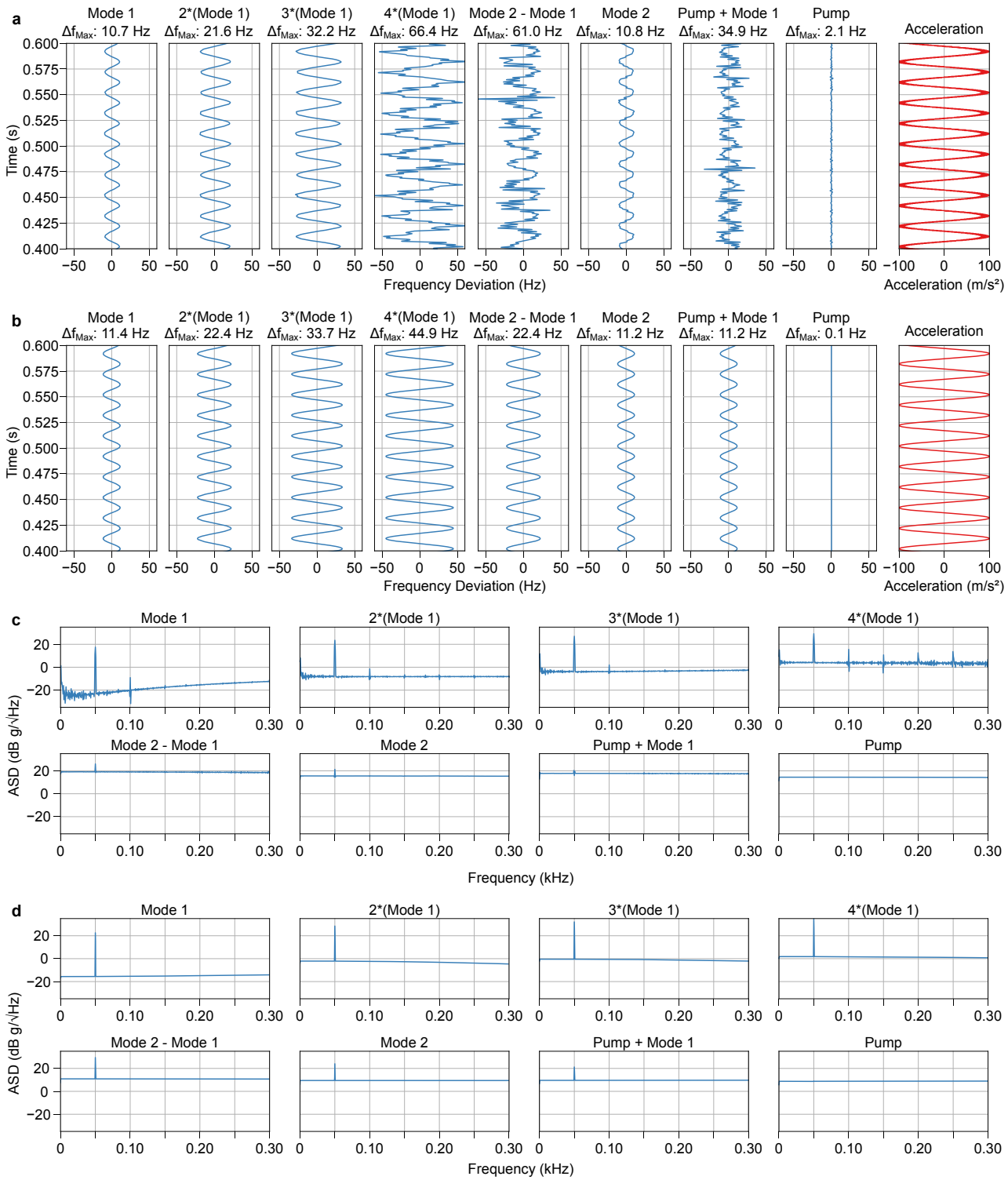


Fig. 6 Per-comb-line FM-demodulation accelerometer results on a calibrated shaker (Device B). Each of panels (**a**–**d**) contains 8 sub-panels, one per comb line, in the order: Mode 1 ($\omega_1/2\pi \approx 3.49\,\mathrm{kHz}$), 2·Mode 1, 3·Mode 1, 4·Mode 1, Mode 2 − Mode 1, Mode 2 ($\omega_2/2\pi \approx 102.70\,\mathrm{kHz}$), Pump + Mode 1, and Pump ($\omega_p/2\pi \approx 106.19\,\mathrm{kHz}$). The pump satisfies $\omega_p \approx \omega_1 + \omega_2$. (**a**) Measured demodulated time-domain frequency-deviation traces for each of the 8 comb lines over 0.40–0.60 s; frequency-deviation axes span ±50 Hz. The Δf_{Max} annotations report the peak excursion of the raw demodulated trace; for the noisier 4·Mode 1 and Mode 2 − Mode 1 lines this exceeds the displayed span, and the acceleration-coherent component is quantified by the 50 Hz peak in (**c**). The rightmost sub-panel shows the simultaneously recorded applied-acceleration trace (red, $\pm 100\,\mathrm{m\,s^{-2}}$, 50 Hz). Deviation amplitude grows approximately linearly with overtone order n, and the Pump sub-panel is flat at the noise floor. (**b**) Simulated demodulated time-domain frequency-deviation traces from the two-mode nonlinear CMT, for the same 8 comb lines and on identical axes as (**a**). (**c**) Measured demodulated frequency-domain spectra of the time traces in (**a**); amplitude spectral density (ASD) in dB ($\mathrm{g}/\sqrt{\mathrm{Hz}}$) on a 0–300 Hz axis. Every mechanical line reproduces the 50 Hz shaker peak; the Pump sub-panel is flat at the noise floor. (**d**) Simulated demodulated frequency-domain spectra from the nonlinear CMT, for the same 8 comb lines and on identical axes as (**c**). The "Pump" sub-panel in (**a**)/(**c**) is flat, with no 50 Hz feature visible, directly demonstrating that the pump itself is not modulated by acceleration; only the mechanical eigenfrequencies ω_1 and ω_2 respond to axial inertial loading.

4 Materials and methods

Device platform and layer stack

The device is a clamped–clamped MEMS bridge with a PZT-on-SOI layer stack and a central proof mass; the bridge footprint is 6.70 mm. The layer stack, bottom-to-top, is: Si handle (450 µm) / SiO_2 buried oxide (BOX, 1 µm) / device Si (14 µm) / Ti adhesion (20 nm) / Pt bottom electrode (150 nm) / PZT (2 µm) / Au top electrode (200 nm) / Si_3N_4 passivation (500 nm). The 2 µm PZT layer is used purely for electromechanical actuation; the mechanical response is read out optically with a Polytec laser Doppler vibrometer (no piezoelectric self-sensing or separate sense electrodes are used in this work). In the clamped–clamped boundary geometry, out-of-plane inertial loading modulates all bending-mode eigenfrequencies through axial mid-plane stretching [24, 25], making every resonant frequency a direct readout of axial load; the central proof mass amplifies the per-g axial-stress sensitivity. Devices A, B and C are nominally identical units from the same platform; only unit-to-unit trim differences separate them.

Measurement: LDV, shaker, and offline FM demodulation

Out-of-plane velocity is measured non-contactly with a Polytec laser Doppler vibrometer (LDV) in single-point and full-field-scanning modes. The parametric pump is a single-tone sinusoid at ω_p delivered to the PZT electrodes via a piezo amplifier; pump frequency and amplitude are swept independently to map the parametric instability landscape. For inertial validation the device is mounted on a calibrated electromagnetic shaker (setup photograph in Supplementary Note S2, Fig. S2); LDV velocity records are post-processed in Python for offline FM demodulation of every comb line. Each comb line is isolated via a matched-filter FIR bandpass (filter shapes shown in Fig. 5a,b) before instantaneous-frequency extraction, and the resulting per-line frequency-deviation time series is what is plotted in Fig. 6a,b. Drive conditions for the accelerometer demonstration: 50 Hz sinusoid, peak acceleration $\approx \pm 100\,\mathrm{m\,s^{-2}}$ ($\approx \pm 10\,g$) at the device, calibrated in-situ with the LDV (see Supplementary Note S2).

Linear TCMT model

Linear modal parameters $\{\omega_n, r_n, C_n\}$ are extracted, for each device, by fitting an N-mode TCMT transmission model to that device's measured small-signal LDV spectrum; the procedure is illustrated on Device A in Fig. 2c and applied identically to Devices B and C. Treating the LDV measurement as a single-port complex transmission $T(\omega)$ of an N-mode linear resonator with a coherent direct-coupling background, the TCMT amplitude equations in the slowly-varying envelope and weak-coupling limit reduce to a sum of complex Lorentzians plus a frequency-independent through term. Each C_n is complex; varying its phase smoothly tunes the line shape between a Lorentzian peak (real-positive C_n), a dip (real-negative C_n), and intermediate asymmetric profiles. Because all line shapes share this single functional form, no per-mode line-shape branching is required. The 18-mode fit reproduces every observable peak in the spectrum across 0–400 kHz. The full derivation is given in Supplementary Note S4.

Nonlinear two-mode CMT and Floquet analysis

The dynamics of MEMS resonators are well described by mass–spring–damping models [32–36]. Under the parametric coupling condition $\omega_p \approx \omega_1 + \omega_2$, the general two-mode coupled-mode equations with quadratic ($\chi^{(2)}$-type) nonlinearity are [16, 37]:

$$\ddot{x}_1 + r_1\dot{x}_1 + \omega_1^2 x_1 + \Gamma\cos(\omega_p t)\, x_2 + \alpha_{11}x_1^2 + \alpha_{12}x_1x_2 = 0, \tag{1}$$

$$\ddot{x}_2 + r_2\dot{x}_2 + \omega_2^2 x_2 + \Gamma\cos(\omega_p t)\, x_1 + \alpha_{22}x_2^2 + \alpha_{21}x_1x_2 = 0, \tag{2}$$

where x_1 and x_2 denote the modal amplitudes of the two interacting modes, the coefficients α_{mn} $(m, n = 1, 2)$ describe the quadratic nonlinearities, and Γ represents the strength of the parametric pumping. Equations (1)–(2) are the model used for all nonlinear numerical simulations in this paper; integration above the parametric threshold reproduces the experimentally observed carrier at ω_2 and sidebands at $\omega_2 \pm n\,\omega_1$ (Fig. 3a,b). For each device the linear frequencies ω_n and damping rates r_n are taken from the TCMT fit of that device's small-signal spectrum (see above); the comb-spectrum simulations of Fig. 3 use the Device-C mode pair ($\omega_1/2\pi \approx 3.61$ kHz, $\omega_2/2\pi \approx 130.11$ kHz).

External acceleration is incorporated into Eqs. (1)–(2) as a slow modulation of the modal stiffnesses. For the clamped–clamped bridge with a central proof mass, an out-of-plane acceleration $a(t)$ exerts an inertial force on the proof mass which is transmitted to the bridge as a uniform axial load through mid-plane stretching; this axial load tension stiffens multiple bending-mode eigenfrequencies. To first order in $a(t)$,

$$\omega_n^2 \;\longrightarrow\; \omega_n^2[\,1 + \eta_n\, a(t)\,], \qquad n = 1, 2, \tag{3}$$

where the fractional stiffness sensitivity $\eta_n \equiv (1/\omega_n^2)\,\partial\omega_n^2/\partial a$ is related to the per-mode frequency scale factor $k_{\mathrm{sf},n}$ (in Hz/g) by $\eta_n \approx 2\,k_{\mathrm{sf},n}/f_n$, with $f_n = \omega_n/2\pi$. Substituting Eq. (3) into Eqs. (1)–(2) yields the working equations used for all FM-response simulations of Fig. 6b,d:

$$\ddot{x}_1 + r_1\dot{x}_1 + \omega_1^2[\,1 + \eta_1\,a(t)\,]\,x_1 + \Gamma\cos(\omega_p t)\,x_2 + \alpha_{11}x_1^2 + \alpha_{12}x_1x_2 = 0, \tag{4}$$

$$\ddot{x}_2 + r_2\dot{x}_2 + \omega_2^2[\,1 + \eta_2\,a(t)\,]\,x_2 + \Gamma\cos(\omega_p t)\,x_1 + \alpha_{22}x_2^2 + \alpha_{21}x_1x_2 = 0. \tag{5}$$

For the calibrated shaker drive of Fig. 6 ($a(t) = a_0\cos(2\pi f_{\mathrm{a}}\,t)$ with $a_0 \approx 100\,\mathrm{m\,s^{-2}} \approx 10\,g$ and $f_{\mathrm{a}} = 50\,\mathrm{Hz}$), the Mode-1 scale factor $k_{\mathrm{sf},1} \approx 1\,\mathrm{Hz/g}$ extracted from the measured carrier deviation in Fig. 6a fixes the Mode-1 stiffness perturbation in Eq. (4) to

$$\omega_1^2\,\eta_1\,a(t)\,x_1 \;\approx\; \omega_1^2\big[\,0.0061\cos(2\pi\cdot 50\,\mathrm{Hz}\cdot t)\,\big]\,x_1, \tag{6}$$

with η_2 set analogously from the Mode-2 modal stress sensitivity. Two features of Eqs. (4)–(5) underpin the FM-only encoding observed in Fig. 6. First, the parametric pump $\Gamma\cos(\omega_p t)$ is itself unmodulated by $a(t)$, so acceleration enters the dynamics only through the parametric modulation of ω_n^2; the time-domain amplitude envelope of every comb line therefore remains flat under varying acceleration, and the encoding is intrinsically frequency-modulated. Second, although the bare eigenfrequencies ω_1 and ω_2 shift in the same direction under axial tension-stiffening (both $\eta_n > 0$), the externally fixed pump enforces $\delta\omega_p = 0$; the locked nonlinear attractor therefore redistributes the modal shift across the comb as $\delta\omega_2^{\mathrm{comb}} = -\delta\omega_1^{\mathrm{comb}}$ between the Mode-1 and Mode-2 carriers, with overtone lines at $n\,\omega_1$ accumulating n copies of the Mode-1 shift. Numerical integration of Eqs. (4)–(5) above the parametric threshold, processed through the same matched-filter / instantaneous-frequency pipeline applied to the experimental LDV records, reproduces the simulated FM panels of Fig. 6b,d and the per-comb-line peak deviations annotated therein.

To extract the parametric instability threshold analytically, we expand to first order the master equations (1)–(2) about the trivial fixed point $\{x_1 = x_2 = 0\}$ and solve the resulting Floquet system. First-order expansion removes every quadratic term, so the linear system below follows directly from Eqs. (1)–(2). For infinitesimal perturbations $x_{1,2} = \Delta_{1,2}$, the linear equations read

$$\ddot{\Delta}_1 + r_1\dot{\Delta}_1 + \omega_1^2\Delta_1 + \Gamma\cos(\omega_p t)\,\Delta_2 = 0, \tag{7}$$

$$\ddot{\Delta}_2 + r_2\dot{\Delta}_2 + \omega_2^2\Delta_2 + \Gamma\cos(\omega_p t)\,\Delta_1 = 0. \tag{8}$$

Equations (7) and (8) constitute a Floquet system [38], whose solutions can be expressed as

$$\Delta_n(t) = \sum_{m=-\infty}^{+\infty} X_{nm}e^{-i(\omega_F + m\omega_p)t} + \mathrm{c.c.}, \tag{9}$$

where $n = 1, 2$ and $\omega_F \in \mathbb{C}$ is the Floquet frequency. The temporal periodicity of the parametric coupling introduces a discrete time-translation symmetry, leading to degenerate solutions of ω_F that differ by integer multiples of ω_p. As a result, all distinct Floquet states can be restricted to the reduced Floquet zone defined by $0 < \mathrm{Re}(\omega_F) < \omega_p$.

The imaginary part of ω_F governs the stability of the zero solution: if $\mathrm{Im}(\omega_F) < 0$ for all eigenvalues, the perturbations decay and the system remains in the off state; if any ω_F satisfies $\mathrm{Im}(\omega_F) > 0$, the corresponding modes grow exponentially. In this regime, the retained nonlinear terms in Eqs. (1)–(2) mix the excited frequencies, generating sidebands spaced by integer multiples of $\mathrm{Re}(\omega_F)$ and thereby forming a frequency comb.

To determine ω_F, we substitute Eq. (9) into Eqs. (7) and (8), yielding the linear system

$$\boldsymbol{J}(\omega_F)\begin{bmatrix}\boldsymbol{X}_1\\ \boldsymbol{X}_2\end{bmatrix} = \boldsymbol{0}, \tag{10}$$

where $\boldsymbol{X}_n$ ($n = 1, 2$) are column vectors with components $[\boldsymbol{X}_n]_m = X_{nm}$. The coefficient matrix $\boldsymbol{J}(\omega_F)$ takes the block form

$$\boldsymbol{J}(\omega_F) = \begin{bmatrix}\boldsymbol{\Omega}_1(\omega_F) & -\boldsymbol{\Gamma}\\ -\boldsymbol{\Gamma} & \boldsymbol{\Omega}_2(\omega_F)\end{bmatrix}. \tag{11}$$

The diagonal blocks $\boldsymbol{\Omega}_n$ are given by $[\boldsymbol{\Omega}_n]_{mk} = \Omega_{nm}\delta_{mk}$, where $\delta_{m,k}$ is the Kronecker delta and

$$\Omega_{nm} = (\omega_F + m\omega_p - z_n)(\omega_F + m\omega_p + z_n^*), \tag{12}$$

$$z_n = \frac{1}{2}\sqrt{4\omega_n^2 - r_n^2} - \frac{i}{2}r_n, \tag{13}$$

where we assume $2\omega_n > r_n$, which is satisfied for the present device. The off-diagonal block $\mathbf{\Gamma}$ contains the Fourier components of the parametric drive $\Gamma\cos(\omega_p t)$,

$$[\mathbf{\Gamma}]_{mk} = \frac{\Gamma}{2}\left(\delta_{m,k+1} + \delta_{m,k-1}\right). \tag{14}$$

The Floquet frequencies are then obtained from the condition

$$\det\left(\boldsymbol{J}(\omega_F)\right) = 0. \tag{15}$$

When $\Gamma = 0$, the matrix $\boldsymbol{J}$ is diagonal, and the Floquet frequencies in the reduced zone reduce to $\omega_F = z_1$ (the root of $\Omega_{1,0}$) and $\omega_F = z_2$ (the root of $\Omega_{2,0}$). As Γ increases, these eigenvalues shift in the complex plane. The instability threshold is reached when one of the Floquet frequencies crosses the real axis. For high-quality-factor modes with $r_1, r_2 \ll \omega_{1,2}$, the threshold pumping amplitude is small. In this regime, $\boldsymbol{J}$ can be truncated to the dominant Fourier components ($m = -1, 0, 1$), yielding

$$\boldsymbol{J}(\omega_F) \approx \begin{bmatrix} \Omega_{1,-1} & 0 & 0 & 0 & -\frac{\Gamma}{2} & 0 \\ 0 & \Omega_{1,0} & 0 & -\frac{\Gamma}{2} & 0 & -\frac{\Gamma}{2} \\ 0 & 0 & \Omega_{1,1} & 0 & -\frac{\Gamma}{2} & 0 \\ 0 & -\frac{\Gamma}{2} & 0 & \Omega_{2,-1} & 0 & 0 \\ -\frac{\Gamma}{2} & 0 & -\frac{\Gamma}{2} & 0 & \Omega_{2,0} & 0 \\ 0 & -\frac{\Gamma}{2} & 0 & 0 & 0 & \Omega_{2,1} \end{bmatrix}. \tag{16}$$

Equation (15) then splits into two branches,

$$\Omega_{2,-1}\Omega_{2,1}\Omega_{1,0} = \frac{\Gamma^2}{4}\left(\Omega_{2,-1} + \Omega_{2,1}\right), \tag{17}$$

or

$$\Omega_{1,-1}\Omega_{1,1}\Omega_{2,0} = \frac{\Gamma^2}{4}\left(\Omega_{1,-1} + \Omega_{1,1}\right). \tag{18}$$

In the limit $\Gamma \to 0$, the solution of Eq. (17) continuously connects to $\omega_F = z_1$, while that of Eq. (18) connects to $\omega_F = z_2$. For the present MEMS device, $r_1 < r_2$, so mode 1 reaches the instability threshold first. Accordingly, the critical Floquet frequency is determined by Eq. (17) as a function of Γ^2, ω_p, and $z_{1,2}$.

In the weak-pumping regime, we expand Eq. (17) in powers of Γ^2 and retain terms up to first order, yielding

$$\omega_F = z_1 + \frac{\Gamma^2}{8z_1}\left[\frac{1}{(z_1 - z_2 + \omega_p)(z_1 + z_2^* + \omega_p)} + \frac{1}{(z_1 + z_2^* - \omega_p)(z_1 - z_2 - \omega_p)}\right], \tag{19}$$

from which the threshold condition $\mathrm{Im}(\omega_F) = 0$ becomes

$$\frac{\Gamma_{\mathrm{th}}^2}{4}\mathrm{Im}\left[\frac{1}{z_1(z_1 - z_2 + \omega_p)(z_1 + z_2^* + \omega_p)} + \frac{1}{z_1(z_1 + z_2^* - \omega_p)(z_1 - z_2 - \omega_p)}\right] = r_1. \tag{20}$$

Equation (20) is plotted as the red curve in Fig. 4a, showing excellent agreement with the edge of the comb region obtained numerically from Eqs. (1) and (2).

In the experiment, the parametric coupling is generated piezo-electrically through a pump voltage V_p. Fig. 4b shows the measured velocity-PSD heatmap in the (ω_p, V_p) parameter space, where the dashed red curve traces the observed threshold separating the no-comb and comb regimes. By mapping this experimentally measured threshold voltage to the analytical threshold $\Gamma_{\mathrm{th}}(\omega_p)$ from Fig. 4a, near the threshold we obtain

$$\Gamma(\omega_p, V_p) \approx \chi_{\mathrm{eff}}(\omega_p)(V_p - V_0), \tag{21}$$

where $V_0 = 1.8$ V is an offset voltage accounting for amplifier calibration uncertainty, imperfect impedance matching, and other experimental nonidealities. The extracted $\chi_{\mathrm{eff}}(\omega_p)$, plotted in Fig. 4c, is a transfer coefficient describing the conversion from the applied pump voltage to the effective parametric coupling strength. The frequency dependence of χ_{eff} arises from the combined response of the entire electromechanical drive chain, with the dominant contribution in the present experiment originating from the frequency response of the amplifier.

Data availability

The source data underlying Figs. 2, 3, 4, 5 and 6 of this study are deposited at https://doi.org/10.5281/zenodo.20267246 and will be made publicly accessible upon journal publication. The deposited record comprises: (i) the laser-Doppler-vibrometry (LDV) velocity time-series and spectra acquired on Device A for the small-signal measurement in Fig. 2(c,d); (ii) the small-signal and above-threshold LDV velocity spectra acquired on Device C (the TCMT-fit input and Fig. 3(c), respectively); (iii) the experimental velocity-PSD map and the analytical/numerical threshold curves shown in Fig. 4(a,b), together with the pump-voltage and pump-frequency cross-section heatmaps of Fig. 4(d,e); (iv) the shaker-input calibration record (50 Hz, $\approx \pm 100\,\mathrm{m\,s^{-2}}$) and the per-comb-line LDV velocity spectra and matched-filter outputs acquired on Device B that feed Fig. 5 and all panels of Fig. 6; (v) the time-domain output of the two-mode nonlinear coupled-mode-theory (CMT) integration used to generate Fig. 3(a,b) and the simulated panels of Figs. 5(b) and 6(b,d); and (vi) the Device-B small-signal LDV measurement feeding Supplementary Note S1 (Fig. S1) and the finite-element sensitivity-sweep data and COMSOL eigenmode field supporting Supplementary Note S3 (Fig. S3). Per-figure source-data files are provided within the same record. Any additional datasets generated during this study are available from the corresponding author on reasonable request.

Code availability

The custom analysis and simulation code used in this study is deposited at https://doi.org/10.5281/zenodo.20267246 together with the underlying data. The deposited record comprises: (i) the Python per-comb-line FM-demodulation pipeline used to produce Figs. 5(a) and 6(a,c); (ii) the numerical integrator for the two-mode nonlinear CMT used to produce Fig. 3(a,b) and the simulated panels of Figs. 5(b) and 6(b,d); and (iii) the analytical truncated-Floquet threshold routine (Eq. (20)) and the numerical phase-diagram routine used to produce Fig. 4(a). Commercial software used in this study comprises MATLAB (MathWorks), COMSOL Multiphysics (linear-elastic eigenmode and axial-load modules), and the Polytec PSV-500 acquisition and analysis software; no modifications were made to these packages.

References

[1] Barbour, N. & Schmidt, G. Inertial sensor technology trends. *IEEE Sensors Journal* **1**, 332–339 (2001).

[2] Seshia, A. A. *et al.* A vacuum packaged surface micromachined resonant accelerometer. *Journal of Microelectromechanical Systems* **11**, 784–793 (2002).

[3] Zhang, Z., Zhang, H., Hao, Y. & Chang, H. A review on MEMS silicon resonant accelerometers. *Journal of Microelectromechanical Systems* **33**, 174–208 (2024).

[4] Saleem, M. M. *et al.* A low-g MEMS accelerometer with high sensitivity, low nonlinearity and large dynamic range based on mode-localization of 3-DoF weakly coupled resonators. *Micromachines* **12**, 310 (2021).

[5] Zotov, S. A., Simon, B. R., Trusov, A. A. & Shkel, A. M. High quality factor resonant MEMS accelerometer with continuous thermal compensation. *IEEE Sensors Journal* **15**, 5045–5052 (2015).

[6] Ren, X., Zhou, X., Yu, S., Wu, X. & Xiao, D. Frequency-modulated MEMS gyroscopes: A review. *IEEE Sensors Journal* **21**, 26426–26446 (2021).

[7] Rugar, D. & Grütter, P. Mechanical parametric amplification and thermomechanical noise squeezing. *Physical Review Letters* **67**, 699–702 (1991).

[8] Turner, K. L. *et al.* Five parametric resonances in a microelectromechanical system. *Nature* **396**, 149–152 (1998).

[9] Liu, Z. *et al.* High-velocity laser Doppler vibrometry measurements on an aluminum nitride bimorph wedge resonator. *Communications Engineering* **5**, 48 (2026).

[10] Udem, T., Holzwarth, R. & Hänsch, T. W. Optical frequency metrology. *Nature* **416**, 233–237 (2002).

[11] Cundiff, S. T. & Ye, J. Colloquium: Femtosecond optical frequency combs. *Reviews of Modern Physics* **75**, 325–342 (2003).

[12] Cao, L. S., Qi, D. X., Peng, R. W., Wang, M. & Schmelcher, P. Phononic frequency combs through nonlinear resonances. *Physical Review Letters* **112**, 075505 (2014).

[13] Ganesan, A., Do, C. & Seshia, A. Phononic frequency comb via intrinsic three-wave mixing. *Physical Review Letters* **118**, 033903 (2017).

[14] Ganesan, A. & Seshia, A. Resonance tracking in a micromechanical device using phononic frequency combs. *Scientific Reports* **9**, 9452 (2019).

[15] de Jong, M. H. J., Ganesan, A., Cupertino, A., Gröblacher, S. & Norte, R. A. Mechanical overtone frequency combs. *Nature Communications* **14**, 1458 (2023).

[16] Park, M. & Ansari, A. Formation, evolution, and tuning of frequency combs in microelectromechanical resonators. *Journal of Microelectromechanical Systems* **28**, 429–431 (2019).

[17] Qi, Z., Menyuk, C. R., Gorman, J. J. & Ganesan, A. Existence conditions for phononic frequency combs. *Applied Physics Letters* **117**, 183503 (2020).

[18] Gobat, G. *et al.* Experimental evidence of mechanical frequency comb in a quad-mass MEMS structure. *2021 IEEE 34th International Conference on Micro Electro Mechanical Systems (MEMS)* 615–618 (2021).

[19] Kumar, P., Chandrashekar, L. N., Jeyaseelan, A. & Pillai, G. Evolution of tunable phononic frequency combs via three-mode interaction in curved piezoelectric micromachined ultrasonic transducers. *Scientific Reports* **15**, 16105 (2025).

[20] Hassani Gangaraj, S. M., Zheng, Y., Wang, J., Park, M. & Ansari, A. High-order harmonics frequency comb generation of a single driven nonlinear NEMS mode. *2024 IEEE 37th International Conference on Micro Electro Mechanical Systems (MEMS)* 537–540 (2024).

[21] Rahmanian, S. *et al.* NEMS generated electromechanical frequency combs. *Microsystems & Nanoengineering* **11**, 8 (2025).

[22] Zhao, Z., Li, Y., Zhang, W., Luo, W. & Liu, D. Acoustic frequency comb generation on a composite diamond/silicon microcantilever in ambient air. *Microsystems & Nanoengineering* **11**, 12 (2025).

[23] Sansa, M. *et al.* Frequency fluctuations in silicon nanoresonators. *Nature Nanotechnology* **11**, 552–558 (2016).

[24] Bouwstra, S. & Geijselaers, B. On the resonance frequencies of microbridges. *TRANSDUCERS '91: International Conference on Solid-State Sensors and Actuators* 538–542 (1991).

[25] Tilmans, H. A. C., Elwenspoek, M. & Fluitman, J. H. J. Micro resonant force gauges. *Sensors and Actuators A: Physical* **30**, 35–53 (1992).

[26] Schmid, S., Villanueva, L. G. & Roukes, M. L. *Fundamentals of Nanomechanical Resonators* (Springer International Publishing, Cham, Switzerland, 2016).

[27] Verbridge, S. S., Parpia, J. M., Reichenbach, R. B., Bellan, L. M. & Craighead, H. G. High quality factor resonance at room temperature with nanostrings under high tensile stress. *Journal of Applied Physics* **99**, 124304 (2006).

[28] Wu, J. *et al.* Self-injection locked and phase offset-free micromechanical frequency combs. *Physical Review Letters* **134**, 107201 (2025).

[29] Roessig, T. A., Howe, R. T., Pisano, A. P. & Smith, J. H. Surface-micromachined resonant accelerometer. *TRANSDUCERS '97: International Conference on Solid-State Sensors and Actuators* 859–862 (1997).

[30] Comi, C. *et al.* A resonant microaccelerometer with high sensitivity operating in an oscillating circuit. *Journal of Microelectromechanical Systems* **19**, 1140–1152 (2010).

[31] Le Traon, O., Janiaud, D., Pernice, M., Muller, S. & Tridera, J.-Y. A new quartz monolithic differential vibrating beam accelerometer. *2006 IEEE/ION Position, Location, And Navigation Symposium (PLANS)* 6–13 (2006).

[32] Younis, M. I., Abdel-Rahman, E. M. & Nayfeh, A. H. A reduced-order model for electrically actuated microbeam-based MEMS. *Journal of Microelectromechanical Systems* **12**, 672–680 (2003).

[33] De, S. K. & Aluru, N. R. Complex nonlinear oscillations in electrostatically actuated microstructures. *Journal of Microelectromechanical Systems* **15**, 355–369 (2006).

[34] Rhoads, J. F., Shaw, S. W. & Turner, K. L. Nonlinear dynamics and its applications in micro- and nanoresonators. *Journal of Dynamic Systems, Measurement, and Control* **132**, 034001 (2010).

[35] Lifshitz, R. & Cross, M. C. in *Nonlinear dynamics of nanomechanical and micromechanical resonators* 1 edn, (ed.Schuster, H. G.) *Reviews of Nonlinear Dynamics and Complexity* 1–52 (Wiley, 2008).

[36] Hajjaj, A. Z., Jaber, N., Ilyas, S., Alfosail, F. K. & Younis, M. I. Linear and nonlinear dynamics of micro and nano-resonators: review of recent advances. *International Journal of Non-Linear Mechanics* **119**, 103328 (2020).

[37] Zhang, W.-M., Meng, G. & Wei, K.-X. Dynamics of nonlinear coupled electrostatic micromechanical resonators under two-frequency parametric and external excitations. *Shock and Vibration* **17**, 759–770 (2010).

[38] Mori, T. Floquet states in open quantum systems. *Annual Review of Condensed Matter Physics* **14**, 35–56 (2023).

Acknowledgements. This work was supported by the Defense Advanced Research Projects Agency (DARPA) under the Higher-Order Composite Resonators for Extra Resilience (HORCREX) program (DARPA-PA-24-04-05). The authors thank S. Bhave and the DARPA program team for their vision in framing the program and for motivating the use of mechanical frequency combs and sensor nonlinearities to pursue inertial sensors that combine high sensitivity, large dynamic range, and resilience to shock and vibration within a single proof mass.

Author contributions. Z.L. and X.N. conceived the project. Z.L. and Y.-C.W. led the experimental work, with X.N. leading the early measurements and E.V. providing experimental support. X.G. developed the analytical model for the parametric-instability threshold (Arnold tongue, Fig. 4a) and reviewed the theoretical sections. Y.-C.W. derived the two-mode coupled-mode theory and led the data post-processing pipeline. Z.L., X.G. and Y.-C.W. performed the data analysis, with contributions from X.N. and E.V. E.V. and M.K. contributed to the theoretical work. S.M. and Y.M. carried out the literature survey. Z.L. drafted the manuscript. A.A. provided critical feedback on the manuscript and project direction. D.B. supervised the project and provided feedback on the manuscript and theory. R.L. acquired funding and supervised the project. N.A.H. supervised the research, secured funding and guided the strategic direction. All authors discussed the results, reviewed the manuscript and approved the final version.

Competing interests. The authors declare no competing interests.

Supplementary Information

The Supplementary Information accompanying this manuscript contains: Supplementary Note S1 (Device-B small-signal LDV measurement in the linear and above-threshold regimes, including the voltage-scaled peak velocities at the Device-B Mode 1 and pump lines that set the FM-transduction operating point, Fig. S1); Supplementary Note S2 (shaker-test setup photograph and LDV-based in-situ calibration of the custom subwoofer-driven shaker, Fig. S2); Supplementary Note S3 (FEM sensitivity sweep illustrating the bridge-thickness scaling and the $t^3 \to t$ crossover into the tension-dominated regime, Fig. S3); and Supplementary Note S4 (linear TCMT model derivation).

Supplementary Files

This is a list of supplementary files associated with this preprint. Click to download.

- SupplementaryNote.docx